

The Cassini VIMS archive of Titan: From browse products to global infrared color maps

S. Le Mouélic^{a,*}, T. Cornet^b, S. Rodriguez^c, C. Sotin^d, B. Seignovert^a, J.W. Barnes^e, R.H. Brown^f, K.H. Baines^d, B.J. Buratti^d, R.N. Clark^g, P.D. Nicholson^h, J. Lasueⁱ, V. Pasek^f, J.M. Soderblom^j

^a Laboratoire de Planétologie et Géodynamique, UMR 6112, CNRS, Université de Nantes, 2 rue de la Houssinière, Nantes 44322, France

^b European Space Astronomy Centre (ESA/ESAC), Villanueva de la Canada, Madrid, Spain

^c IPGP, CNRS-UMR 7154, Université Paris-Diderot, USPC, Paris, France

^d Jet Propulsion Laboratory, California Institute of Technology, 4800 Oak Grove Drive, Pasadena, CA 91109, USA

^e Department of Physics, University of Idaho, Engineering-Physics Building, Moscow, ID 83844, USA

^f Department of Planetary Sciences, University of Arizona, Tucson, AZ 85721, USA

^g Planetary Science Institute, Tucson, USA

^h Department of Astronomy, Cornell University, Ithaca, NY 14853, USA

ⁱ IRAP, Toulouse, France

^j MIT, Department of Earth, Atmospheric and Planetary Sciences, Cambridge, MA 02139, USA

ARTICLE INFO

Keywords:

Titan
Titan surface
Image processing
Infrared observations

ABSTRACT

We have analyzed the complete Visual and Infrared Mapping Spectrometer (VIMS) data archive of Titan. Our objective is to build global surface cartographic products, by combining all the data gathered during the 127 targeted flybys of Titan into synthetic global maps interpolated on a grid at 32 pixels per degree (~ 1.4 km/pixel at the equator), in seven infrared spectral atmospheric windows. Multispectral summary images have been computed for each single VIMS cube in order to rapidly identify their scientific content and assess their quality. These summary images are made available to the community on a public website (vims.univ-nantes.fr). The global mapping work faced several challenges due to the strong absorbing and scattering effects of the atmosphere coupled to the changing observing conditions linked to the orbital tour of the Cassini mission. We determined a surface photometric function which accounts for variations in incidence, emergence and phase angles, and which is able to mitigate brightness variations linked to the viewing geometry of the flybys. The atmospheric contribution has been reduced using the subtraction of the methane absorption band wings, considered as proxies for atmospheric haze scattering. We present a new global three color composite map of band ratios (red: 1.59/1.27 μm ; green: 2.03/1.27 μm ; blue: 1.27/1.08 μm), which has also been empirically corrected from an airmass (the solar photon path length through the atmosphere) dependence. This map provides a detailed global color view of Titan's surface partially corrected from the atmosphere and gives a global insight of the spectral variability, with the equatorial dunes fields appearing in brownish tones, and several occurrences of bluish tones localized in areas such as Sinlap, Menvra and Selk craters. This kind of spectral map can serve as a basis for further regional studies and comparisons with radiative transfer outputs, such as surface albedos, and other additional data sets acquired by the Cassini Radar (RADAR) and Imaging Science Subsystem (ISS) instruments.

1. Introduction

Titan has been recognized since the era of the Voyager space missions as one of the most interesting bodies in the field of comparative planetology. Although the surface is totally masked in the visible wavelength by scattering and absorptions in the atmosphere, the geological diversity of Titan has been progressively revealed by the

instruments onboard the Cassini spacecraft, which spent 13 years between 2004 and 2017 in the Saturnian system. The Radar instrument onboard Cassini was able to observe directly through Titan's atmosphere using a centimetric wavelength (Elachi et al., 2005). Optical observations were performed by two other instruments. The Imaging Science Subsystem (ISS), composed of two multispectral framing cameras, provided information on the surface thanks to its 0.93 μm CB3

* Corresponding author.

E-mail address: stephane.lemouelic@univ-nantes.fr (S. Le Mouélic).

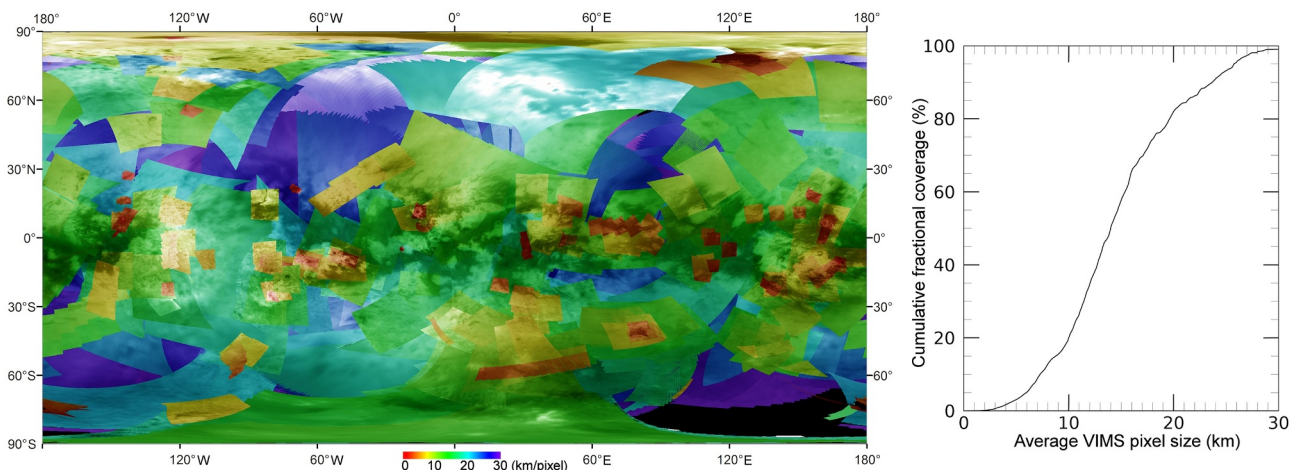


Fig. 1. Pixel size (in km) of the cubes used to build our global mosaic. A global map at 2 μm is shown in transparency. The cumulative fractional coverage is shown on the right. Only 5% of the surface has been observed with a pixel size better than 6 km. 60% was observed in conditions better than 15 km/pixels.

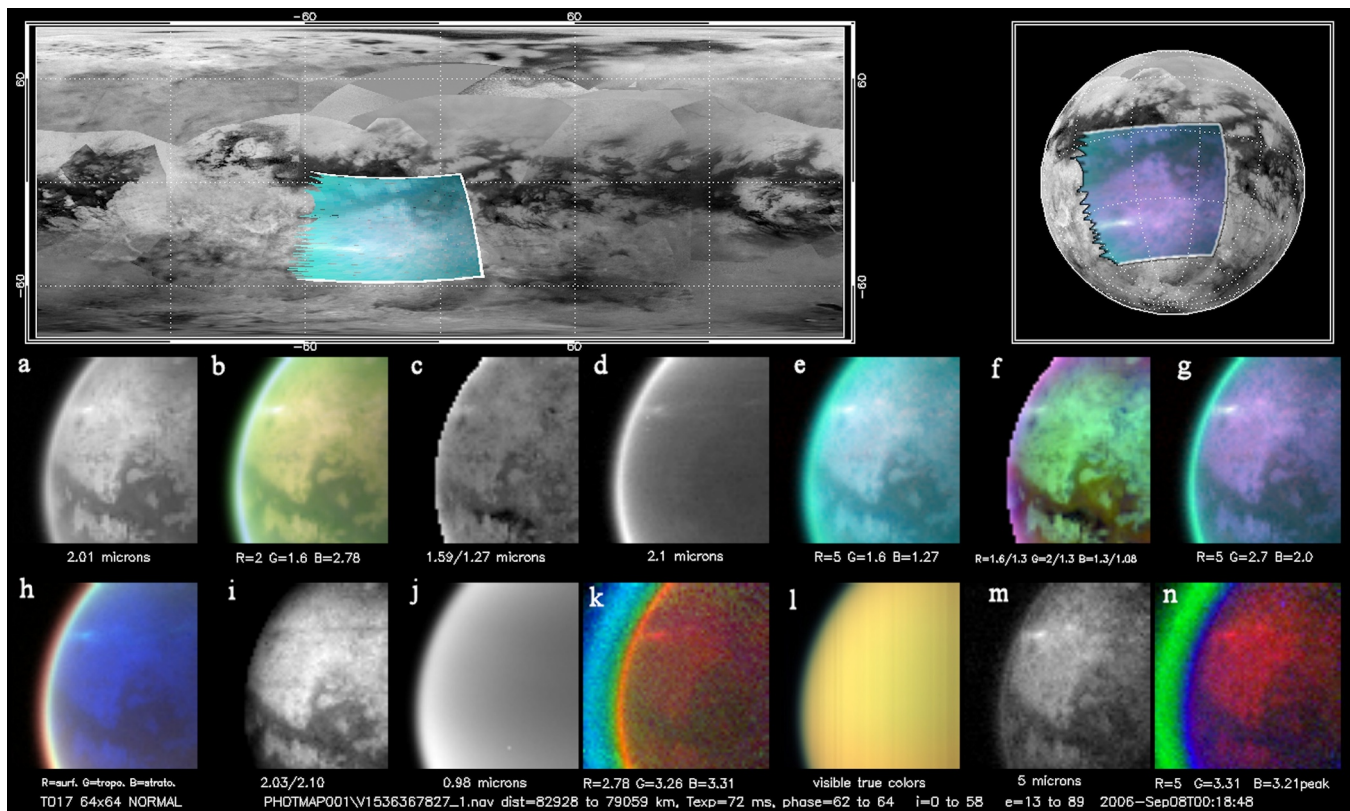


Fig. 2. Example of VIMS multispectral summary image on cube CM_1536367827 (8 September 2006). Black and white images and color composites have been designed to catch variations linked both to surface and atmospheric features.

filter (Porco et al., 2005). The Visual and Infrared Mapping Spectrometer (VIMS) acquired hyperspectral images which gave access to the surface through partially transparent atmospheric windows in the infrared at 1.08, 1.27, 1.59, 2.01, 2.69, 2.78 and 5 μm (Brown et al., 2004; Sotin et al., 2005). The spectral dimension of VIMS provides the possibility to retrieve information on compositional and/or physical state (grain size) variations at the surface, in addition to giving access to clouds and aerosols properties. With observations collected year after year, the geological diversity of Titan proved to be exceeding the most optimistic expectations. Earth-like processes and landforms such as cloud formation, river flowing at the surface (implying rainfalls), polar lakes and seas, mountain chains, equatorial dunes fields, impact craters, were progressively discovered and characterized (Tomasko et al. 2005;

Stofan et al., 2007; Radebaugh et al., 2007, 2008; Wood et al., 2010; Aharonson et al., 2014). The main difference with Earth comes from the nature of the materials: with an average surface temperature of -180°C , methane is close to its triple point, playing on Titan the role of water on Earth. Only very few impact craters have been observed on the entire surface (Wood et al., 2010), which indicates that the surface is geologically relatively young, probably reprocessed by tectonic events, erosion of the bedrock, and deposition of sediments from air fall or slope/fluvial transport processes (Neish et al., 2016; Brossier et al., 2018).

In this paper, we focus our study on the VIMS global archive, with the objective of producing global color mosaics of the complete data set of Titan acquired between T0 (July 2004) and the last targeted flyby,

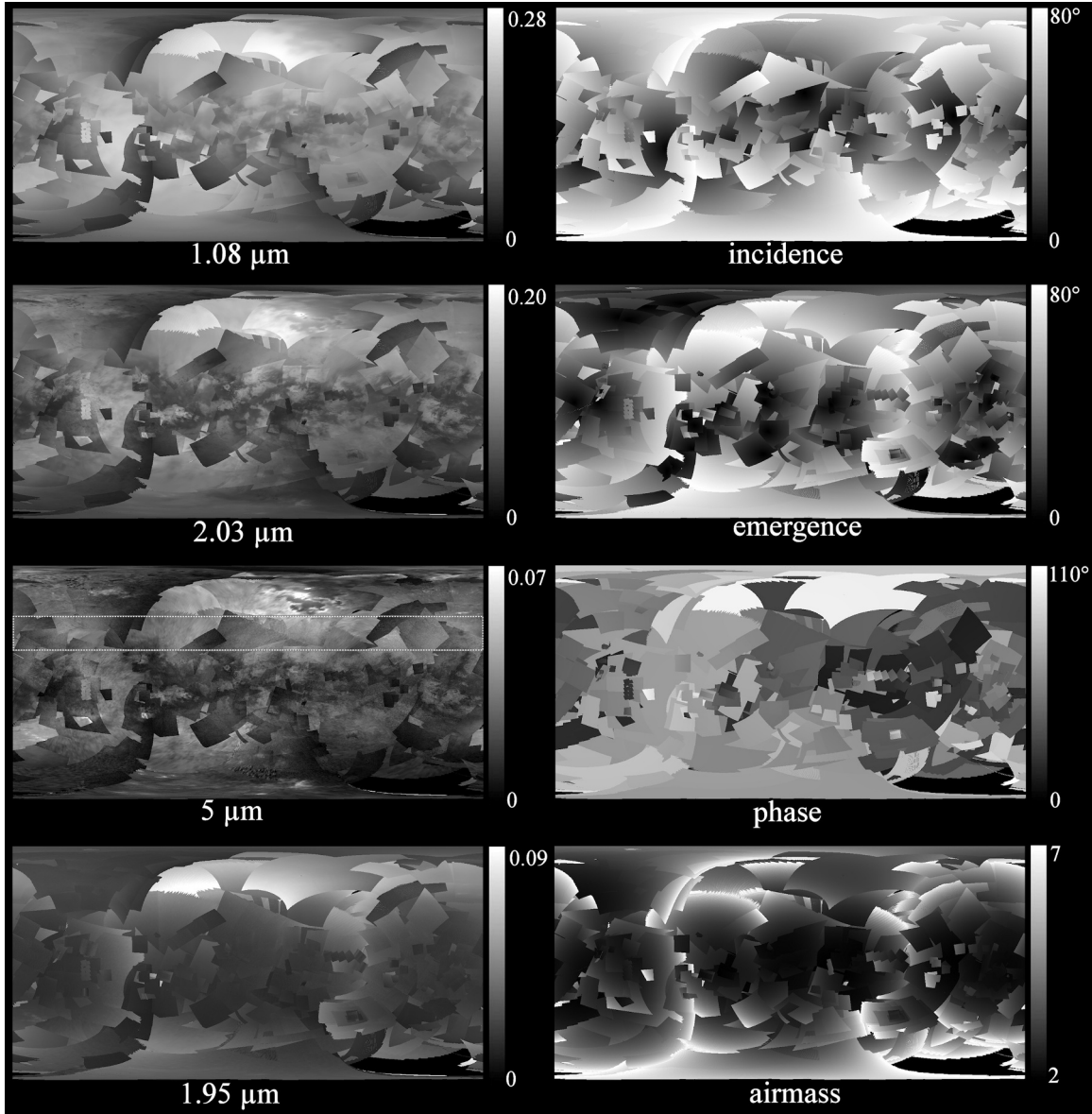


Fig. 3. Raw global mosaics in equidistant cylindrical projection at 1.08, 2.03, 5 μm (surface windows) and 1.95 μm (atmosphere only) compared to global mosaics of incidence, emergence, phase, and airmass, containing all the VIMS cubes acquired during the entire Cassini mission, within the data filters described in the text. The observing conditions vary widely during the mission, which causes significant seams or boundaries to appear in the uncorrected mosaics. The white dashed rectangle on the 5 μm map corresponds to the test area used to determine the corrections.

T126, in April 2017. The correspondence between the Cassini flybys of Titan and the Cassini orbits around Saturn can be found in Seignovert (2015). We consolidate a previous study, which was limited to data acquired up to June 2010 only (Le Mouélic et al., 2012a). Merging data acquired in very different viewing conditions into global homogeneous maps is a challenge due to the presence of the atmosphere, which induces strong absorbing and scattering effects when coupled with the changing geometry of the flybys. In a first section, we describe the global VIMS data set, its observing modes and radiometric calibration, and discuss the production of multispectral summary images designed to catch the scientific content of each observation in an optimized way. In a second step, we present how the data were merged into global maps, after implementing empirical corrections for the surface photometry and for the atmospheric effects. We discuss in particular the use of band ratios, before concluding with series of orthographic views and a focus on the Huygens landing site.

2. Description of the VIMS data set

2.1. VIMS observing modes

The Visual and Infrared Mapping Spectrometer (VIMS) onboard Cassini acquired up to 64×64 pixels images in 352 spectral channels from 0.35 to 5.12 μm (Brown et al., 2004). VIMS was composed of two separate instruments. The first was a two-dimension CCD array that covers the visible range (0.35–1.04 μm) with 96 spectral channels. The second covered the infrared range (0.88–5.12 μm) with 256 channels on a linear detector array and a bidirectional mirror (whisk-broom). The visible part has proved to be very challenging to observe the surface of Titan, due to the strongly absorbing and scattering atmosphere (Tomasko et al., 2005; Hirtzig et al., 2009; Vixie et al., 2012). Since we focus our present study on surface observations, we therefore center our efforts on the infrared detector. Between 2004 and 2017, hyperspectral data have been gathered during 127 targeted Titan close encounters, in addition to more distant untargeted observations. The spatial size of

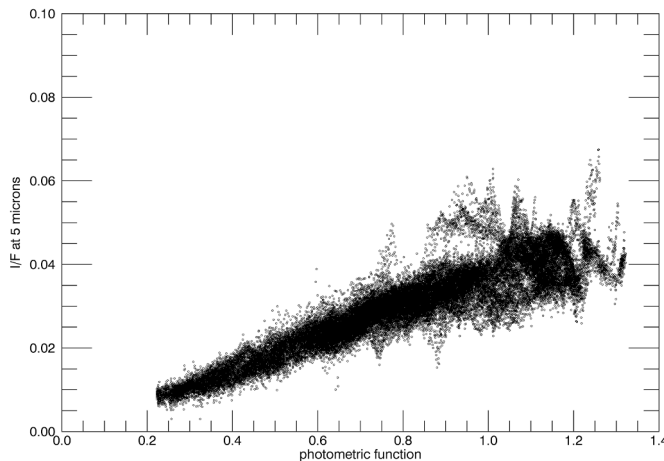


Fig. 4. I/F at 5 μm versus the photometric function described in Eq. (1). The linear correlation shows that this function can be used to correct at first order from the effect of incidence, emergence and phase.

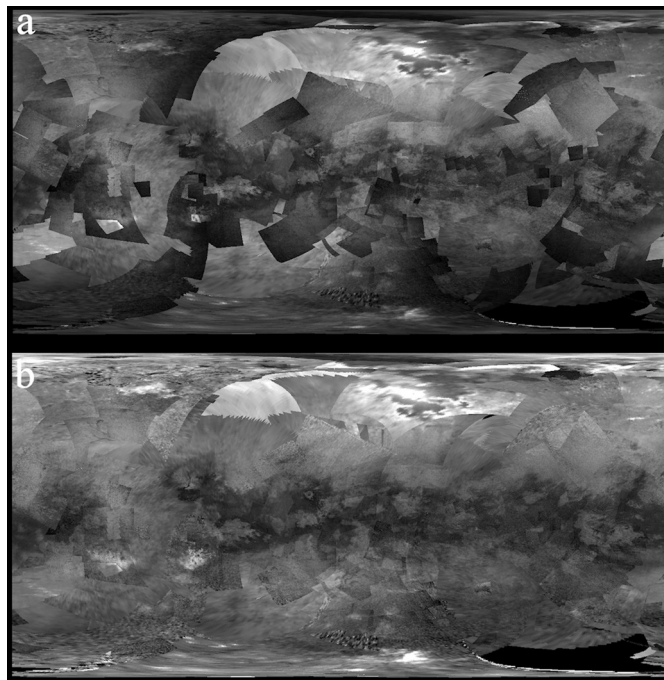


Fig. 5. (a) Uncorrected global map at 5 μm . (b) 5- μm map corrected using the surface photometric function described in Eqs. (1) and (2). Most of the seams have been smoothed out, except on two cubes in northern regions, one of which exhibiting a broad specular reflexion on Kraken Mare.

data cubes were optimized to take advantage of any acquisition opportunities, which relied on which instrument was driving the pointing of Cassini during the closest approach phase. Occasionally, cubes were acquired on a line mode (“noodle”), letting the spacecraft drift build the second dimension of the image after concatenation of a series of hundreds of line cubes. An occultation mode was also designed to catch the signal of stars crossing Titan’s atmosphere. The time exposure generally ranged from 13 ms (used mostly at closest approach to compensate the fast drift of the surface) to 640 ms (when a higher S/N ratio was desired to look for subtle spectral signatures at long wavelengths). More than 60,000 hyperspectral cubes of Titan have been acquired during the entire Cassini mission, with a pixel size as fine as 500 m at best when VIMS was operating right at closest approach in very few occasions. Fig. 1 shows the spatial coverage obtained with all cubes acquired within thresholds that we describe in a later stage to build the mosaics,

with pixel sizes smaller than 30 km and with time exposures in the 20–300 ms range to avoid low signal to noise ratios and saturated cubes. The panel on the right displays the corresponding cumulative fractional coverage. The region around (80°S, 120°E), which represents ~1% of the surface, was never observed within these thresholds. Only 5% of the surface was covered with a pixel scale lower than 6 km/pixel. The cumulative global coverage raises to 20% when considering observations better than the 10 km/pixel scale, and 60% for observations better than the 15 km/pixel scale.

2.2. Radiometric calibration

All the data cubes have been calibrated in reflectance factor I/F, where F is the solar flux (irradiance) and I is the calibrated radiance measured by VIMS. We followed the VIMS pipeline described in Brown et al. (2004) and Barnes et al. (2007), and further refined using a time-dependent radiometric calibration aimed at correcting a small wavelength shift that has been identified during the last years of the mission (Clark et al., 2018). Up to ~10 nm of progressive shift is observed when comparing data taken in 2004 and data taken in 2017 (Clark et al., 2018). Despite this shift being small, it can dramatically alter the surface information in the sharp atmospheric windows (especially at short wavelength), and produce significant seams if left uncorrected. In the last calibration step, all spectra of the mosaic have therefore been converted to a common reference wavelength of 2004 with a spline interpolation, using the shifts evaluated by Clark et al. (2018).

2.3. VIMS multispectral summary products

For each VIMS hyperspectral cube of Titan (except the single line cubes and the cubes taken in occultation mode), we have setup a multispectral summary image designed to highlight the spectral diversity of the observation using specific combination of channels, and displaying the cubes under different map projections. This strategy is similar to the one used by the Compact Reconnaissance Imaging Spectrometer for Mars (CRISM) team to automatically search for mineral signatures on Mars (Pelkey et al., 2007). It allows us to visually find the most interesting data, in addition to identify corrupted cubes. Fig. 2 shows an example on a typical multispectral summary product acquired at T17 in September 2006. We choose to display both enhanced black and white and color composites which are dedicated either to surface or atmospheric features. We use for example the 2.01 μm channel (Fig. 2a) to emphasize the details of the surface. We also calculated three RGB composites of single bands inspired from previous studies (Barnes et al., 2007; Soderblom et al., 2009a; Le Mouélic et al. 2012a), which reveal at the same time clouds and surface features (Fig. 2b, e and g). The 1.59/1.27 μm ratio (Fig. 2c) emphasizes spectral variations of the surface. The image acquired at 2.1 μm (Fig. 2d) is used to detect clouds (Rodriguez et al., 2009, 2011; Turtle et al., 2018), which appear bright at this wavelength where the surface is not seen. Fig. 2f corresponds to an RGB color composite of the 1.59/1.27 μm , 2.03/1.27 μm and 1.27/1.08 μm band ratios respectively, which provide the most sensitivity to surface heterogeneities. We included in Fig. 2h a color composite with the surface, tropospheric and stratospheric parameters of Brown et al. (2010). The 2.03/2.10 μm ratio (Fig. 2i) provides a tentative normalization of the illuminating conditions. The image acquired at 0.98 μm (Fig. 2j) shows a pure atmospheric scattering observation. We have added two color composites ($R = 2.78 \mu\text{m}$, $G = 3.26 \mu\text{m}$, $B = 3.31 \mu\text{m}$ in Fig. 2k and $R = 5 \mu\text{m}$, $G = 3.31 \mu\text{m}$, $B = 3.21 \mu\text{m}$ in Fig. 2n) which are sensitive to the methane fluorescence and reveal the layers of the atmosphere. A true color image is also displayed (Fig. 2l). Finally, the image acquired at 5 μm (Fig. 2m) corresponds to the average of all channels between 4.90 and 5.12 μm . This wavelength range is the least affected by atmospheric scattering. Information regarding the flyby number, date, distance

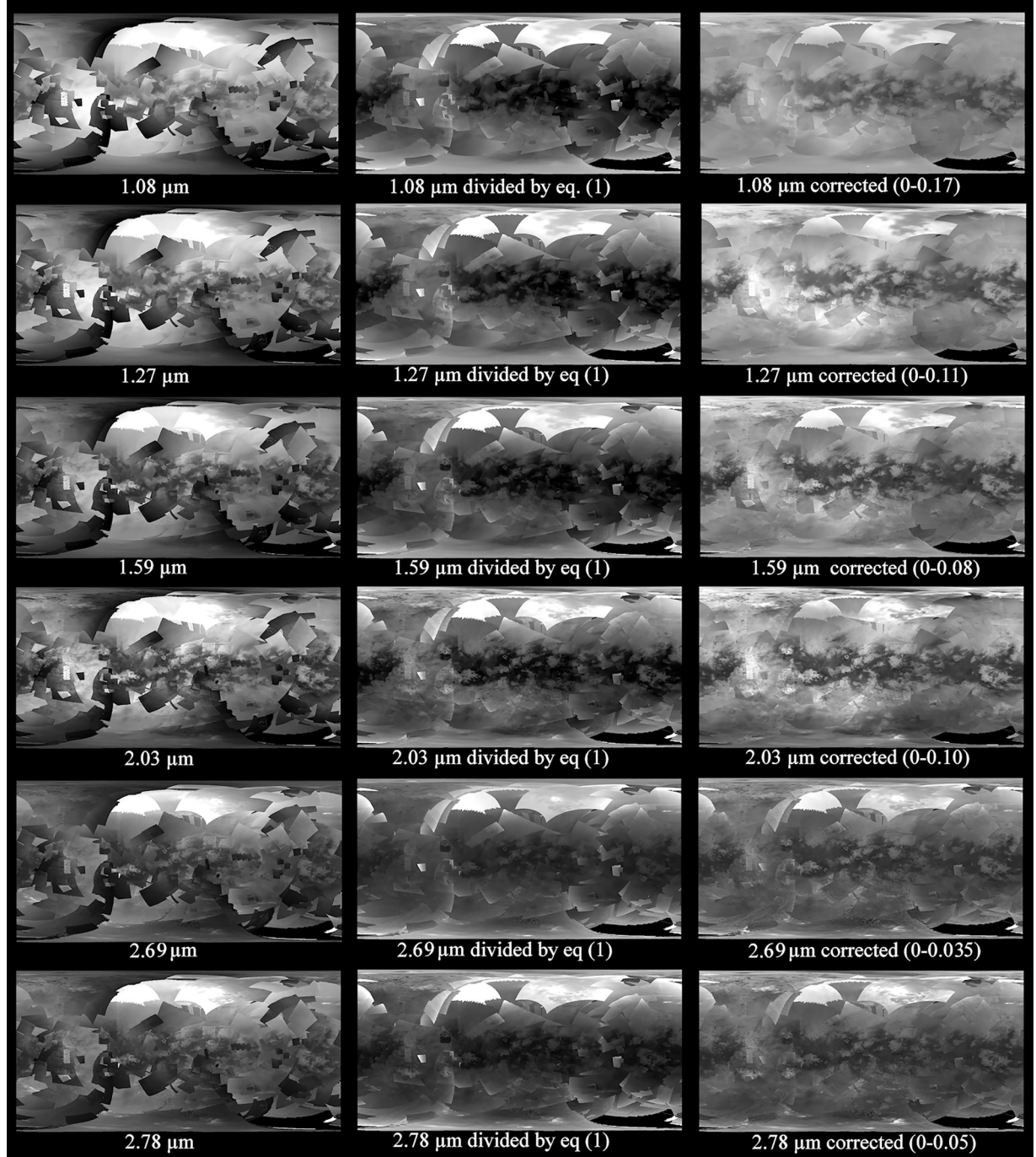


Fig. 6. Mosaics at 1.08, 1.27, 1.59, 2.03, 2.69, 2.78 μm without correction (left), with a photometric correction only (center), and with the first order correction of the additive scattering term prior to the photometric correction (right).

range of Cassini to Titan's surface at the time of the cube acquisition, pixel exposure time, ranges for the phase, incidence and emergence angles is also displayed.

The browse products contain a wealth of information that could potentially stimulate further focused atmospheric and surface studies. A dedicated website has been setup to provide a user-friendly access to all these multispectral summary images, produced from the Planetary Data System archive and covering the entire mission (vims.univ-nantes.fr).

3. Merging data into global maps

Our final objective is to produce VIMS synthetic global maps interpolated on a grid at 32 pixels per degree (corresponding to a spatial

sampling of $\sim 1.4 \text{ km}$ at the equator), using different combinations of wavelengths emphasizing surface spectral heterogeneities. Merging 13 years of data represents a significant challenge considering the non-negligible contribution of Titan's absorbing and scattering atmosphere even in the methane optical windows, the huge variations in observing conditions encountered throughout the mission, as well as the temporal changes that could have occurred in the surface and atmosphere during 13 years (Barnes et al., 2013b; Solomonidou et al., 2016).

3.1. Data fusion strategy

In order to build global maps, individual data cubes have been sorted by increasing spatial resolution, with the high resolution images

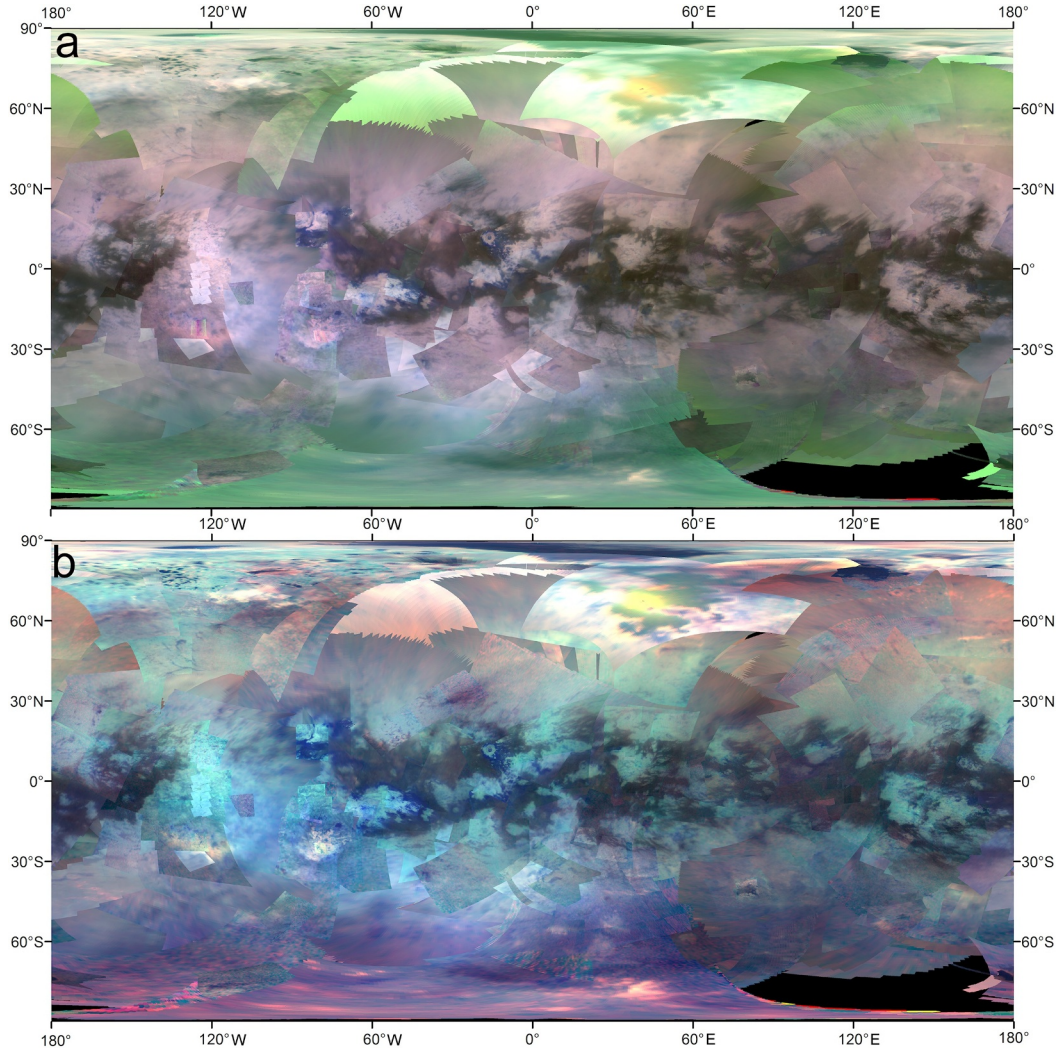


Fig. 7. (a) RGB global map with the red, green and blue controlled by the 2.0, 1.59 and 1.27 μm channels respectively. (b) RGB global map with the red, green and blue controlled by the 5, 2.0 and 1.27 μm channels respectively. (For interpretation of the references to colour in this figure legend, the reader is referred to the web version of this article.)

on top of the mosaic and the low resolution images used as background. Other strategies could be envisaged to give more weight to other parameters influencing data quality, such as time exposure or low airmass (that we defined by $1/\cos i + 1/\cos e$ in the plane-parallel atmosphere approximation), instead of the spatial resolution only (i.e., Barnes et al., 2007). After testing this approach, we decided to keep the spatial resolution as the main criterion to emphasize the finest details of the surface. We filtered out the observing geometry in order to remove the pixels acquired in too extreme illuminating and viewing conditions, which produce strong seams in the VIMS mosaics due to enhanced surface and atmospheric photometric effects. We used thresholds of 80° both on the incidence and emergence angles, 110° on the phase angle, and 7 on the airmass. These thresholds correspond to a trade-off between the surface coverage (in particular in polar areas, most often viewed at extreme geometries) and the mosaic quality. The lowest values of the incidence, emergence, phase and airmass in the mosaic are 0.12°, 0.02°, 11.1°, 2.01 respectively. The exposure time has been restrained to the 20–300 ms range in order to avoid cubes with low signal-to-noise ratio and saturated data.

Fig. 3 shows the resulting global mosaic of relevant geometric viewing parameters (incidence, emergence, phase and airmass), the I/F at 1.08, 2.03 and 5 μm (surface windows), the I/F at 1.95 (where the atmosphere is not transparent) with no correction for geometry nor for

the atmospheric effects. Many boundaries or seams appear between individual images in these raw mosaics. They are mainly caused by the varying viewing angles (incidence, emergence, phase) between data acquired during the different flybys, which induce strong atmospheric and surface photometric effects. A dependence with airmass is also observed. Other discrepancies might exist due to surface and atmospheric temporal variations, and residual calibrations artifacts.

3.2. Photometric correction at 5 μm

In order to account for the variations of solar illumination (incidence i) and viewing angle (emergence e) between different flybys, a surface photometric correction had to be implemented. We focused on the 5 μm atmospheric window, which is the least affected by atmospheric scattering and absorption, and thus is the most sensitive to surface photometric effects. We selected a test area presenting a rather homogeneous brightness at 5 μm , located in the Northern mid-latitudes between 37.5° N and 52.5° N (white dashed rectangle in the 5 μm map of Fig. 3), outside of the lakes, seas, or dune fields. Given the relatively weak atmospheric absorption and haze scattering in this window, most of the variations seen in this portion of the mosaic come from the viewing conditions of the surface.

We have tested several surface photometric corrections commonly

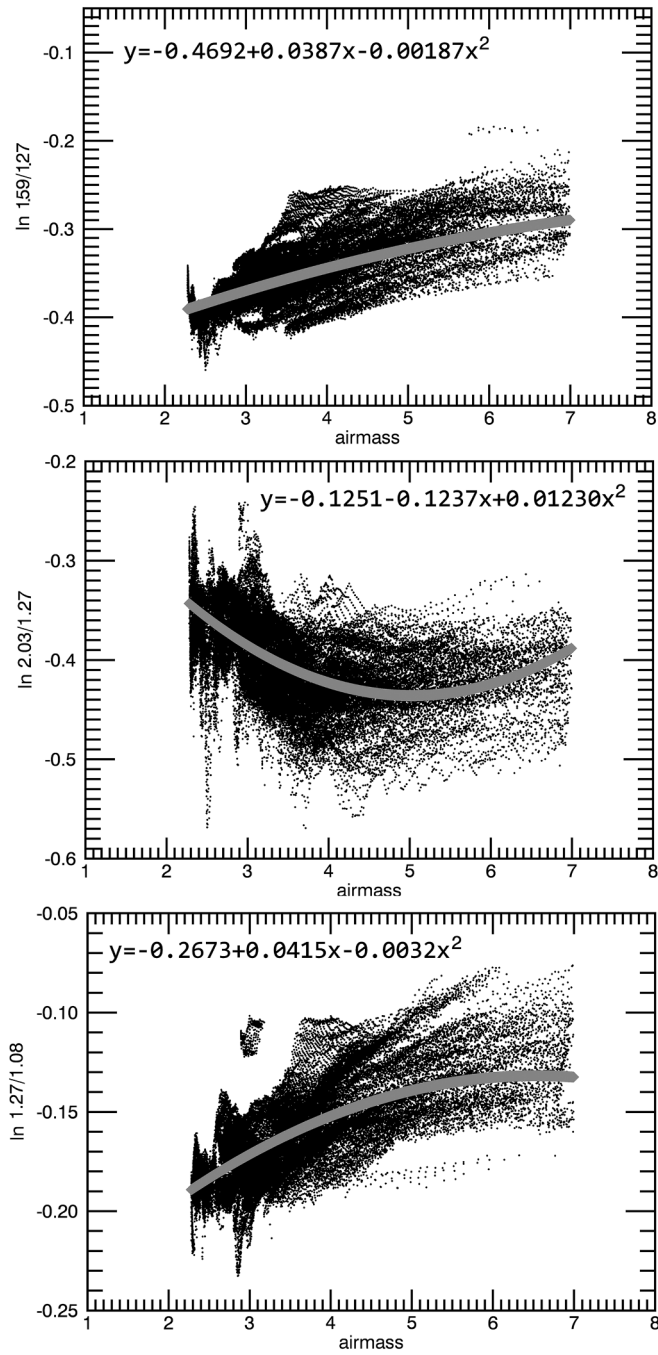


Fig. 8. Dependence of band ratios with airmass on the test area containing mostly homogeneously bright terrains located in the latitudinal belt between 37.5° N and 52.5° N. A positive correlation is observed for the upper and lower panels, whereas the middle panel presents a negative correlation at low airmass values. This dependence can be empirically corrected at first order using a second order polynomial fit.

found in the literature. These include the Lambert, Lommel-Seeliger and Lunar Lambert disc functions, coupled with different particle phase functions $P(\phi)$ such as the Rayleigh, Henyey-Greenstein and Hapke lunar functions (Hapke et al., 2012). While particle phase functions are usually used to infer particle shape and size properties (e.g., Henyey-Greenstein two lobes phase function), we rather focus on the mosaic enhancement, the phase function giving us an indication of the degree of anisotropy in scattering. Whereas a pure Lambert function gave satisfactory results to perform a first order correction of the incidence angle (i) in an earlier version of the maps (Le Mouélic et al., 2012a), we

realized that a supplementary correction of the emergence (e) and phase (ϕ) angles was needed to account for the extreme diversity of the viewing conditions, in particular on the northern polar regions, which were only seen during the second half of the Cassini mission after the dissipation of the northern cloud and haze (Le Mouélic et al., 2012b, 2018). These areas were not included in our previous maps. Our best result was obtained with a Lunar Lambert type function (Eqs. (1) and (2)) with a lunar-like weighting factor $A = 0.285$ (Figs. 4 and 5).

$$f = A \cos i / (\cos i + \cos e) \times P(\phi) + (1 - A) \times \cos i \quad (1)$$

$$P(\phi) = \frac{4\pi}{5} \left[\frac{\sin \phi + (\pi - \phi) \cos \phi}{\pi} + \frac{(1 - \cos \phi)^2}{10} \right] \quad (2)$$

$P(\phi)$ in Eq. (1) is the single-particle phase function of the surface. The lunar theoretical particle phase function of Hapke (1963) provided satisfactory results to describe this term (Eq. (2)), as it was already noted by Cornet et al. (2012). The fact that the point cloud in Fig. 4 is aligned with the origin of the graph confirms the hypothesis that the additive scattering term at 5 μm is negligible.

The uncorrected map at 5 μm is shown in Fig. 5a. The map at 5 μm corrected for the photometry with the factor described in Eqs. (1) and (2) is shown in Fig. 5b. We see that the level of seams has significantly decreased in almost all regions, except two cubes in northern latitudes taken in an extreme geometry and which contain in particular a broad specular reflexion on Kraken Mare. Very bright features in this map correspond to possible evaporites (Barnes et al., 2011; McKenzie et al., 2014), specular reflections on the northern seas (Sotin et al., 2012; Soderblom et al., 2012; Barnes et al., 2013a; Barnes et al., 2014), possible cryovolcanic candidates (Lopes et al., 2013), or unfiltered clouds (Turtle et al., 2018).

In the following, we will use the same photometric function for all other surface windows, assuming that the surface properties are not wavelength-dependent. This is a shortcoming, as a complete solution would require to derive different photometric parameters for each wavelength, as it is commonly done for example on bodies such as Mars (Binder and Jones, 1972) and the Moon (Lane and Irvine, 1973). However, to achieve this, the contribution of the atmosphere on Titan has to be fully removed prior to the photometric parameters computation, which still makes it very challenging at this stage, and falls beyond the scope of this paper. We leave this issue to further studies based on complete radiative transfer approaches.

3.3. Short wavelengths case

Whereas the 5 μm methane window is almost free of atmospheric scattering, this is not the case for wavelengths shorter than 3 μm, which contain an additive scattering contribution of the aerosols. To mitigate this effect, we use the wings of the atmospheric windows as a proxy to correct for the amount of additive scattering present in the center of these windows, where the surface is seen by VIMS. This process is already described in Le Mouélic et al. (2012a) and will therefore not be fully reproduced here. We used the same set of k-factor (values of 1.15, 1.50, 1.60, 1.29 and 1.14 respectively for the 1.08, 1.27, 1.59, 2.03 and 2.78 μm atmospheric windows, e.g., Table 1 in Le Mouélic et al., 2012a), which account for the difference of transparency between the center of the windows and their wings. The wings were taken at 1.03, 1.14, 1.22, 1.32, 1.49, 1.65, 1.95, 2.13, 2.64 and 2.83 μm. These wavelengths correspond to the first images (departing from the center of the windows) for which no surface feature is visually detectable in the global mosaic, even at the lowest airmass conditions. The 2.69 μm image is corrected with the same wings and k-factor as the 2.78 μm image, as these two windows correspond to a double peak rather than a single narrow one.

Fig. 6 presents a comparison of the maps in the surface windows before (left column) and after this empirical atmospheric correction process (right column). The middle column shows partial results, where

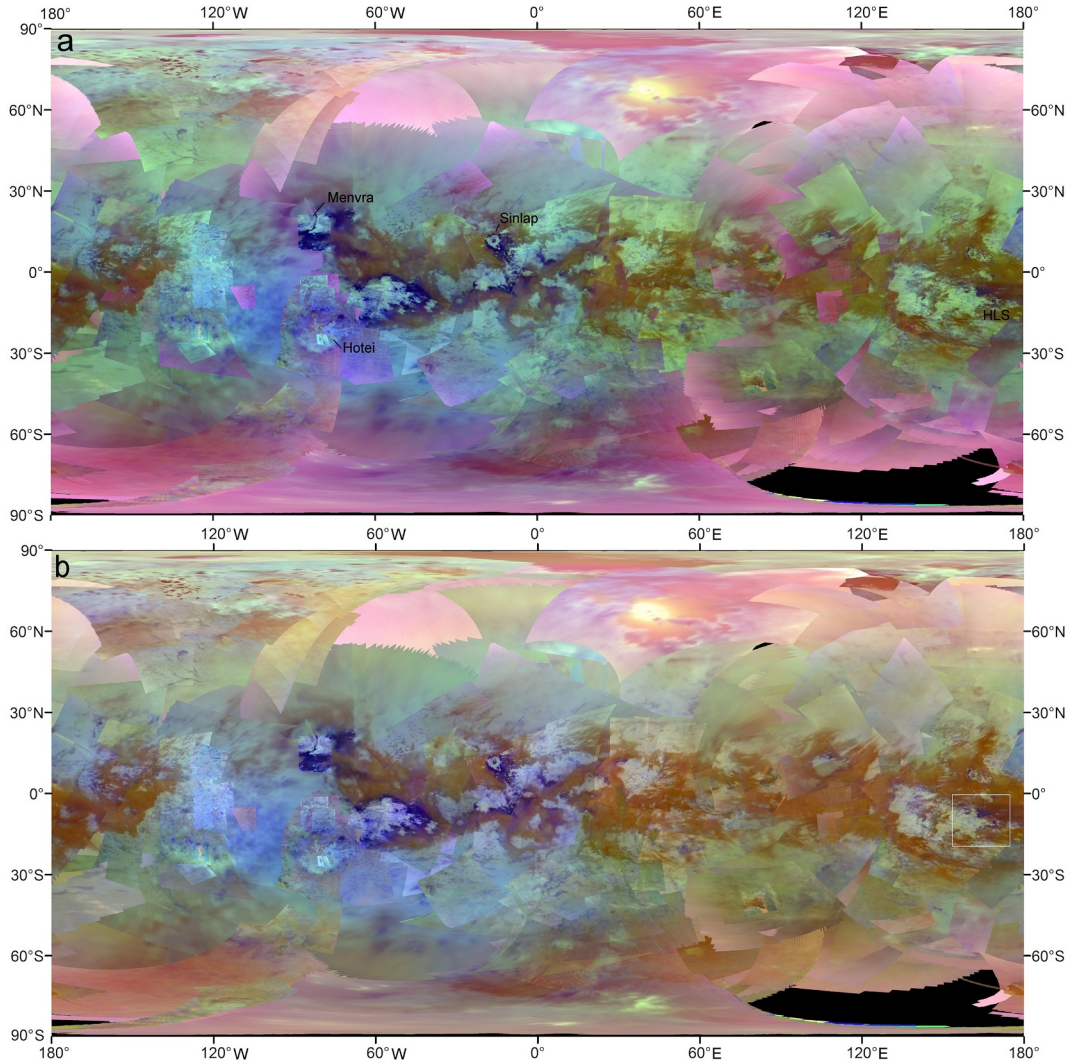


Fig. 9. (a) RGB color map with the red, green and blue channels controlled by the 1.59/1.27, 2.03/1.27 and 1.27/1.08 μm ratios respectively. (b) Same mosaic after the empirical correction of the airmass dependence Eqs. (3)–(5)). The correction decreases the contrast at the seams due to the atmosphere at the equator and near the poles. The white rectangle shows the location of the zoom on the Huygens landing site displayed in Fig. 11. (For interpretation of the references to colour in this figure legend, the reader is referred to the web version of this article.)

only the surface photometric correction described in Section 3.2 has been applied without the subtraction of the band wings, which would be the typical correction for data acquired on an airless body. The level of residual seams has been decreased in all the windows in most cases after the complete correction process (right column).

In order to emphasize spectral variations linked to compositional heterogeneities, the maps in Fig. 6 can be combined into RGB color composites. Fig. 7 shows two RGB global color maps. Fig. 7a has been coded with the red, green and blue channels controlled respectively by the 2.01, 1.59 and 1.27 μm mosaics empirically corrected from atmospheric scattering and photometry with the method described above. Fig. 7b corresponds to a global mosaic with the red, green and blue channels controlled by the 5, 2.01 and 1.27 μm images respectively. Introducing the 5 μm window decreases the level of the greenish trend seen in Fig. 7a due to the residual absorption and scattering in the atmosphere, mainly in the polar regions. A broad specular reflexion is seen on Kraken Mare in both cases.

These color composites have been widely used in regional studies (e.g., Barnes et al., 2007, 2011; Soderblom et al., 2009a, 2009b; Cornet et al., 2012; Rodriguez et al., 2014). Our objective is now to go one step further by investigating band ratios, which are extremely sensitive to subtle spectral variations, as it has already been shown in the case of

airless bodies.

3.4. Color composites of band ratios

To better emphasize spectral heterogeneities, we also computed RGB composites of band ratios. Band ratios, which cancel out all multiplicative factors in absence of additive components, is a powerful technique widely used in planetary sciences. For Titan, the 1.59/1.27 μm , 2.03/1.27 μm and 1.27/1.08 μm ratios proved to be useful for localized regional studies (Le Mouélic et al., 2008; Brossier et al., 2018). However, using band ratios on global maps of Titan still remains very challenging, as ratios are generally much more sensitive to atmospheric effects and any residual calibration artifacts than RGB composites of single bands only. Producing fully artifact-free global maps of band ratios would still be some sort of ultimate cartographic product that requires a thorough investigation of the residuals present in the corrected mosaics.

In order to make progress in this direction, we investigated the dependence of the ratios with geometric parameters. We observed in particular that the logarithm of each ratio appears correlated with our airmass parameter, so with the amount of atmosphere that the light has been crossing. This is illustrated in the scatter plots of Fig. 8,

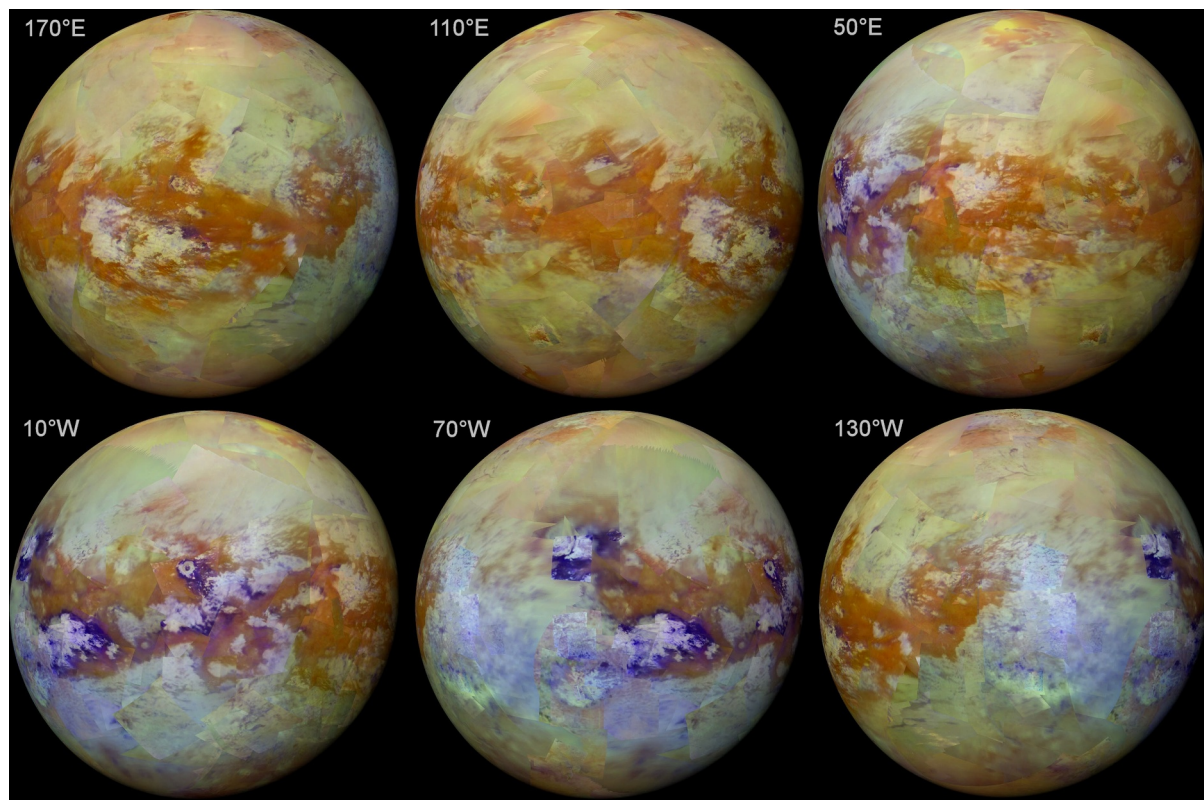


Fig. 10. Selection of orthographic views derived from the RGB corrected color ratio map of Fig. 9b after a last cosmetic hand cleaning step. The upper left image is centered at $(0^\circ, 170^\circ\text{E})$, close to the Huygens landing site. The six panels correspond to views where Titan is rotated by 60° in longitude eastward from left to right and from top to bottom. The equatorial dune fields appear readily in brown. Bright terrains and several patches of bluish areas also show up in specific locations. (For interpretation of the references to colour in this figure legend, the reader is referred to the web version of this article.)

corresponding to all the points located in our test latitudinal belt between 37.5°N and 52.5°N , containing mostly homogeneously bright terrains. The dependence of the ratios with the airmass is also apparent when comparing the RGB composite of the $1.59/1.27\text{ }\mu\text{m}$, $2.03/1.27\text{ }\mu\text{m}$ and $1.27/1.08\text{ }\mu\text{m}$ ratios in Fig. 9a and the airmass map in Fig. 3. This is particularly the case in fuzzy pinkish areas seen near the equator in Fig. 9a.

Following the systematic trends observed in Fig. 8, we decided to empirically remove this dependence with airmass using a second order polynomial fit derived on the scatter plot of the logarithm of the ratios versus the airmass. The corresponding correction formula are given below:

$$\left(\frac{R_{1.59}}{R_{1.27}}\right)_{\text{corrected}} = \left(\frac{R_{1.59}}{R_{1.27}}\right) e^{-(0.0387a - 0.00187a^2)} \quad (3)$$

$$\left(\frac{R_{2.03}}{R_{1.27}}\right)_{\text{corrected}} = \left(\frac{R_{2.03}}{R_{1.27}}\right) e^{(-0.1237a + 0.0123a^2)} \quad (4)$$

$$\left(\frac{R_{1.27}}{R_{1.08}}\right)_{\text{corrected}} = \left(\frac{R_{1.27}}{R_{1.08}}\right) e^{(-0.0415a - 0.0032a^2)} \quad (5)$$

where R_λ is the reflectance at the wavelength λ and “a” is the airmass defined by $1/\cos(i) + 1/\cos(e)$. After this purely empirical step, the resulting RGB color composite of band ratios appears much less dependent on the geometry of observations, as shown in Fig. 9b. Whereas this map still contains some dependence with atmospheric contributions and pure brightness variations, subtle color differences are strongly emphasized compared to previous RGB maps due to the use of the ratios. The strongly diffusing atmosphere still hampers the study of the polar areas (appearing in pink), but the ratios nicely reveal the extent of equatorial dune fields, which appear in brownish tones.

Fig. 9b is so far the most advanced global cartographic product that we have been able to automatically produce. Fig. 10 shows a series of orthographic views centered on the equator, with a point of perspective at infinite distance, derived from this map after a last minor cosmetic hand cleaning step. The six panels correspond to hemispheric views where Titan is rotated by 60° in longitude eastward from left to right and from top to bottom. One of the most striking feature is the equatorial dune fields (Radebaugh et al., 2008; Rodriguez et al., 2014), which appear readily in brownish tones. The second main spectral type of interest corresponds to dark blue areas such as the ones we see around Sinlap and Menvra craters, or north east of Hotei Regio. This color difference can be spectrally explained by a local enrichment in water ice, decreasing the reflectance at 1.59 and $2.01\text{ }\mu\text{m}$ compared to the $1.27\text{ }\mu\text{m}$ channel (Rodriguez et al., 2006; McCord et al., 2008; Solomonidou et al., 2018; Brossier et al., 2018). However, we point out that this interpretation is not unique, as several organic compounds could potentially create the same spectral effect. Indeed, many organics show the downward trend with increasing wavelength like water ice (e.g., Clark et al., 2009, 2010; Kokaly et al., 2017a, 2017b). NH-bearing compounds show an even stronger downward trend than water ice. Discriminating between these compositional signatures will require a very precise atmospheric removal and analysis of the detailed spectral structure within each window, which is still an ongoing field of research. Our main objective here was rather to show the global distribution of spectral heterogeneities itself. We leave the identification of individual constituents to further dedicated studies, which could rely both on laboratory spectra and detailed radiative transfer modeling, and which fall beyond the scope of this paper. We now give a regional example of the color map in one of the most important spot on Titan: the Huygens landing site.

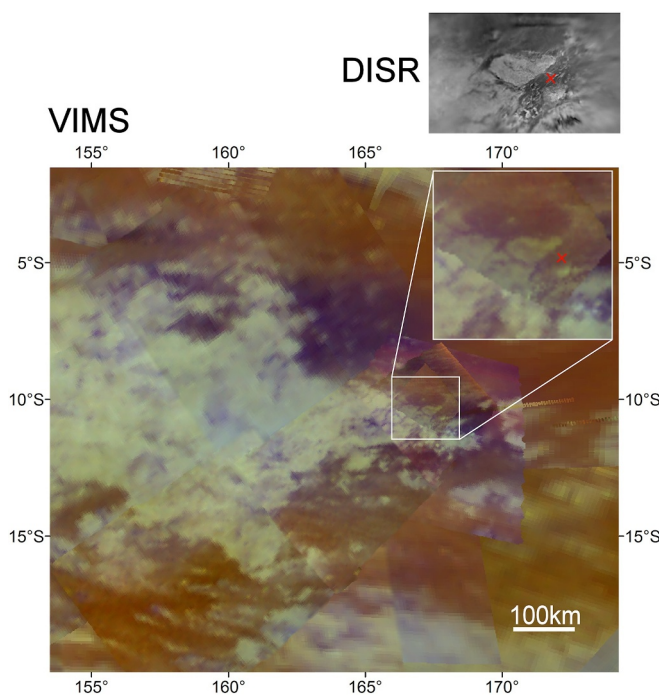


Fig. 11. Detail of the VIMS color ratio map corresponding to the area in the white square in Fig. 9b. The Huygens landing site is marked by a red cross. A black and white panorama acquired by DISR on Huygens from an altitude of ~34 km is shown for comparison (top). We can easily recognize the bright feature north of the landing site in both data sets. VIMS suggests that Huygens landed in an area corresponding to the moderate bluish tone units. (For interpretation of the references to colour in this figure legend, the reader is referred to the web version of this article.)

3.5. Zoom on the Huygens landing site

In order to illustrate the accuracy of the final band ratio map, Fig. 11 shows a zoom on the Huygens landing site. This area is the only spectral measurement acquired from the surface and is therefore of particular interest. The first VIMS observation acquired at T_a in October 2004 (cube CM_1477491859) had a spatial sampling of 14 km/pixel and provided the general context (Rodriguez et al., 2006). The best observation of the landing site itself has then been acquired at T47 in November 2008 (cube labeled CM_1605804042), when VIMS was operating at closest approach. This allowed to acquire an observation in a spot pointing mode, with the whole spacecraft spinning progressively to compensate for the fast drift of the surface. The spatial sampling of the T47 cube ranged between 0.75 and 1.4 km per pixel. Other late observations provided the intermediate context. They were acquired at T88 in November 2012 (cube CM_1732874866, between 2.1 and 2.7 km /pixel) and T85 in July 2012 (cube CM_1721856031, between 3.2 and 5.5 km/pixel).

In Fig. 11, we see that all these data have been homogeneously merged into the color band ratio map, despite being acquired with different geometries and with a time span of eight years. It appears that the Huygens probe landed in an area which corresponds to moderately bluish tones. The accuracy of the VIMS observation is sufficiently high to easily recognize the bright dissected terrain that was imaged by the DISR camera at an altitude of ~34 km during the descent of Huygens under its parachute (Tomasko et al., 2005; Karkoschka and Schröder, 2016). Further studies could be considered to perform a detailed comparison between the VIMS cubes mentioned here and the DISR data, following the work of Karkoschka and Schröder (2016).

4. Conclusion

We have reduced the global VIMS hyperspectral archive of Titan integrating data from T₀ to T126 flybys in order to map the spectral heterogeneities at the surface. Multispectral summary images have been computed for each hyperspectral VIMS cube, in order to give an easy access to the scientific content of each observation. These browse products are available on the vims.univ-nantes.fr website. Based on automatic filters and manual refinement in the cube selection using these summary images, ~19,000 individual data cubes have then been merged to produce global color maps at 32 pixels per degree (~1.4 km/pixel at the equator) in the seven atmospheric methane optical windows. We implemented a correction for the surface photometric function which takes into account the incidence, emergence, and phase variations. An empirical subtraction of the band wings is used to mitigate the effects of the additive scattering aerosols at short wavelengths. We also investigated band ratios, a powerful technique to emphasize subtle spectral variations, by implementing an empirical correction of the absorption difference between the ratioed channels. This process allowed us to build global maps which integrate data from the complete mission and which strongly emphasize the global distribution of the main spectral units. In particular, the band ratio global map readily shows the extent of the equatorial dune fields (which appears in brown tones in band ratio RGB composites of the 1.59/1.27, 2.03/1.27 and 1.27/1.08 μm channels). Several areas show a dark bluish color, such as near Sinlap, Menvra or Selk craters for example, due to a change in composition and/or grain size.

The residual discrepancies in the maps are due to several factors. One of the challenges comes from temporal variations at the surface (Barnes et al., 2013b; Solomonidou et al., 2016) and moreover in the atmosphere (haze and clouds). This is particularly true at the poles, where significant changes occurred during the mission (Le Mouélic et al., 2018). The north pole was fully covered by haze and cloud up to ~55°N at the beginning of the mission. We had to wait for the circulation turnover after the equinox in 2009 to get clearer skies in the north. The south pole experienced a reverse situation, with clear skies at the beginning of the mission and a polar cloud appearing after 2012 and growing in size up to 2017. In addition to these polar events, sporadic methane clouds have been observed throughout all the mission (e.g., Rodriguez et al., 2009, 2011; Turtle et al., 2018).

The surface photometric behavior can be improved in further studies using a more complex photometric function using wavelength-dependent parameters. This will require a better decorrelation between atmospheric and surface contributions in the methane windows. More inputs derived from a complete radiative transfer analysis could also provide another way to improve the homogeneity of the maps in future works (Cornet et al., 2017).

Acknowledgments

Authors are very grateful to two anonymous reviewers for their very detailed comments. This work has been partly funded by the French spatial agency (CNES). We also acknowledge the financial support from Région Pays de la Loire, project GeoPlaNet (convention 2016-10982). S.R. is supported by the Institut Universitaire de France and acknowledges support from the UnivEarthS LabEx program of Sorbonne Paris Cité (ANR-10-LABX-0023, ANR-11-IDEX-0005-02) and the French National Research Agency (ANR-APOSTIC-11-BS56-002, ANR-12-BS05-001-3/EXO-DUNES).

Supplementary materials

Supplementary material associated with this article can be found, in the online version, at doi:10.1016/j.icarus.2018.09.017.

References

- Aharonson, O., Hayes, A.G., Haynes, P.O., Lopes, R.M., Lucas, A., Perron, J.T., 2014. Titan's Surface geology, in Titan. In: Müller-Wodarg, I., Griffith, C.A., Lellouch, E., Cravens, T.E. (Eds.), Cambridge University Press, Cambridge, UK.
- Barnes, J.W., Brown, R.H., Soderblom, L., Buratti, B.J., Sotin, C., Rodriguez, S., Le Mouélic, S., Baines, K.H., Clark, R., Nicholson, P., 2007. Global-scale surface spectral variations on Titan seen from Cassini/VIMS. *Icarus* 186, 242–258.
- Barnes, J.W., Bow, J., Schwartz, J., Brown, R.H., Soderblom, J.M., Hayes, A.G., Vixie, G., Le Mouélic, S., Rodriguez, S., Sotin, C., Jaumann, R., Stephan, K., Soderblom, L.A., Clark, R.N., Buratti, B.J., Baines, K.H., Nicholson, P.D., 2011. Organic sedimentary deposits in Titan's dry lakesbeds: probable evaporite. *Icarus* 216 (Issue 1), 136–140. <https://doi.org/10.1016/j.icarus.2011.08.022>.
- Barnes, J.W., Clark, R.N., Sotin, C., Adamkovics, M., Appérè, T., Rodriguez, S., Soderblom, J.M., Brown, R.H., Buratti, B.J., Baines, K.H., Le Mouélic, S., Nicholson, P.D., 2013a. A transmission spectrum of Titan's north polar atmosphere from a specular reflection of the Sun. *Astrophys. J.* 777, 161. <https://doi.org/10.1088/0004-637X/777/2/161>.
- Barnes, J.W., Buratti, B.J., Turtle, E.P., Bow, J., Dalba, P.A., Perry, J., Brown, R.H., Rodriguez, S., Le Mouélic, S., Baines, K.H., Sotin, C., Lorenz, R.D., Malaska, M.J., McCord, T.B., Clark, R.N., Jaumann, R., Hayne, P.O., Nicholson, P.D., Soderblom, J.M., Soderblom, L.A., 2013b. Precipitation-induced surface brightenings seen on Titan by Cassini VIMS and ISS. *Planet. Sci.* 2, 1. <https://doi.org/10.1186/2191-2521-2-1>.
- Barnes, J.W., Sotin, C., Soderblom, J.M., Brown, R.H., Hayes, A.G., Buratti, B.J., Rodriguez, S., Le Mouélic, S., Baines, K.H., McCord, T.B., Clark, R.N., Nicholson, P.D., 2014. Cassini/VIMS observes rough surfaces on Titan's Punga Mare in specular reflection. *Planet. Sci.* 3, 3. <https://doi.org/10.1186/s13535-014-0003-4>.
- Binder, A.B., Jones, J.C., 1972. Spectrophotometric studies of the photometric function, composition and distribution of the surface materials of Mars. *J. Geophys. Res.* 77, 3005–3020. <https://doi.org/10.1029/JB077i017p03005>.
- Brown, R.H., et al., 2004. The Cassini visual and infrared mapping spectrometer (VIMS) investigation. *Space Sci. Rev.* 115, 111–168.
- Brown, M.E., Roberts, J.E., Schaller, E.L., 2010. Clouds on Titan during the Cassini prime mission: a complete analysis of the VIMS data. *Icarus* 205 (2), 571–580. <https://doi.org/10.1016/j.icarus.2009.08.024>.
- Brossier, J.F., Rodriguez, S., Cornet, T., Lucas, A., Radebaugh, J., Maltagliati, L., Le Mouélic, S., Solomonidou, A., Coustenis, A., Hirtzig, M., Jaumann, R., Stephan, K., Sotin, C., 2018. Geological evolution of Titan's equatorial regions: possible nature and origin of the dune material. *J. Geophys. Res.* <https://doi.org/10.1029/2017JE005399>.
- Brown, R.H., et al., 2004. The Cassini visual and infrared mapping spectrometer investigation. *Space Sci. Rev.* 115, 111–168.
- Clark, R.N., Curchin, J.M., Hoefen, T.M., Swayze, G.A., 2009. Reflectance spectroscopy of organic compounds I: alkanes. *J. Geophys. Res.* 114, E03001. <https://doi.org/10.1029/2008JE003150>.
- Clark, R.N., Curchin, J.M., Barnes, J.W., Jaumann, R., Larry Soderblom, Cruikshank, D.P., Brown, R.H., Rodriguez, S., Lunine, J., Stephan, K., Hoefen, T.M., Le Mouélic, S., Sotin, C., Baines, K.H., Buratti, B., Nicholson, P., 2010. Detection and mapping of hydrocarbon deposits on Titan. *J. Geophys. Res.* 115, E10005. <https://doi.org/10.1029/2009JE003369>.
- Clark, R.N., R.H. Brown, D.M. Lytle, Hedman, M., The VIMS wavelength and radiometric calibration 19, Final Report, NASA Planetary Data System, The Planetary Atmospheres Node, 30p. The Planetary Atmospheres Node, Direct link: https://pds-imaging.jpl.nasa.gov/data/cassini/cassini_orbiter/vims-calibration-files/, 2018.
- Cornet, T., Bourgeois, O., Le Mouélic, S., Rodriguez, S., Lopez Gonzalez, T., Sotin, C., Tobie, G., Fleurant, C., Barnes, J.W., Brown, R.H., Baines, K.H., Buratti, B.J., Clark, R.N., Nicholson, P.D., 2012. Geomorphological significance of Ontario Lacus on Titan: integrated interpretation of Cassini VIMS, ISS and RADAR data and comparison with the Etosha Pan (Namibia). *Icarus* 218 (2), 788–806. <https://doi.org/10.1016/j.icarus.2012.01.013>.
- Cornet, T., Rodriguez, S., Maltagliati, L., Appérè, T., Sotin, C., Le Mouélic, S., Rannou, P., Solomonidou, A., Hirtzig, M., Bézard, B., Coustenis, A., Brown, R.H., Barnes, J.W., Baines, K.H., Buratti, B.J., Clark, R.N., Nicholson, P.D., 2017. Radiative transfer modelling in Titan's atmosphere: application to Cassini/VIMS data. In: 48th LPSC, abstract#1847.
- Elachi, C., et al., 2005. Cassini radar views the surface of Titan. *Science* 308 (5724), 970–974. <https://doi.org/10.1126/science.1109919>.
- Hapke, B.W., 1963. A theoretical photometric function for the lunar surface. *J. Geophys. Res.* 68, 4571–4586.
- Hapke, B., Denevi, B., Sato, H., Braden, S., Robinson, M., 2012. The wavelength dependence of the lunar phase curve as seen by the Lunar Reconnaissance Orbiter wide-angle camera. *J. Geophys. Res.* 117.
- Hirtzig, M., Tokano, T., Rodriguez, S., Le Mouélic, S., Sotin, C., 2009. A review of Titan's atmospheric phenomena. *Astron. Astrophys. Rev.* 17 (Issue 2), 105–147. <https://doi.org/10.1007/s00159-009-0018-0>.
- Karkoschka, E., Schröder, S., 2016. Eight-color maps of Titan's surface from spectroscopy with Huygens' DISR. *Icarus* 270, 260–271. <https://doi.org/10.1016/j.icarus.2015.06.010>.
- Kokaly, R.F., Clark, R.N., Swayze, G.A., Livo, K.E., Hoefen, T.M., Pearson, N.C., Wise, R.A., Benzel, W.M., Lowers, H.A., Driscoll, R.L., Klein, A.J., 2017a. USGS Spectral Library Version 7: U.S. Geological Survey Data Series. <https://doi.org/10.3133/ds1035>.
- Kokaly, R.F., R.N. Clark, G.A. Swayze, K.E. Livo, T.M. Hoefen, N.C. Pearson, R.A. Wise, W. M., Benzel, H.A. Lowers, R.L. Driscoll, and A.J. Klein, 2017, USGS Spectral Library Version 7 Data: U.S. Geological Survey data release, doi:[10.5066/F7RR1WDJ](https://doi.org/10.5066/F7RR1WDJ)
- (<https://speclab.cr.usgs.gov/spectral-lib.html>).
- Lane, A.P., Irvine, W.M., 1973. Monochromatic phase curves and albedos for the lunar disk. *Astron. J.* 78, 267. <https://doi.org/10.1086/111414>.
- Le Mouélic, S., Paillou, P., Janssen, M.A., Barnes, J.W., Rodriguez, S., Sotin, C., Brown, R.H., Baines, K.H., Buratti, B.J., Clark, R.N., Crapeau, M., Encrenaz, P., Jaumann, R., Geudtner, D., Paganelli, F., Soderblom, L., Tobie, G., Wall, S., 2008. Mapping and interpretation of Sinlap crater on Titan using Cassini VIMS and RADAR data. *J. Geophys. Res.* 113, E04003. <https://doi.org/10.1029/2007JE002965>.
- Le Mouélic, S., Cornet, T., Rodriguez, S., Sotin, C., Barnes, J.W., Baines, K.H., Brown, R.H., Lefèvre, A., Buratti, B.J., Clark, R.N., Nicholson, P.D., 2012a. Global mapping of Titan's surface using an empirical processing method for the atmospheric and photometric correction of Cassini/VIMS images. *Planet. Space Sci.* 73 (1), 178–190. <https://doi.org/10.1016/j.pss.2012.09.008>.
- Le Mouélic, S., Rannou, P., Rodriguez, S., Sotin, C., Griffith, C., Le Corre, L., Barnes, J.W., Brown, R.H., Baines, K., Buratti, B., Clark, R., Nicholson, P., Tobie, G., 2012b. Dissipation of Titan's north polar cloud at northern spring equinox. *Planet. Space Sci.* 60, 86–92. <https://doi.org/10.1016/j.pss.2011.04.006>.
- Le Mouélic, S., Rodriguez, S., Robidel, B., Rousseau, B., Seignovert, B., Sotin, C., Barnes, J.W., Brown, R.H., Baines, K.H., Buratti, B.J., Clark, R.N., Nicholson, P.D., Rannou, P., Cornet, T., 2018. Mapping polar atmospheric features with VIMS: from the dissipation of the northern cloud to the onset of the southern polar vortex. *Icarus* 311, 371–383. <https://doi.org/10.1016/j.icarus.2018.04.028>.
- Lopes, R.M.C., Kirk, R.L., Mitchell, K.L., Le Gall, A., Barnes, J.W., Hayes, A., Kargel, J., Wye, L., Radebaugh, J., Stofan, E.R., Janssen, M.A., Neish, C.D., Wall, S.D., Wood, C.A., Lunine, J.I., Malaska, M.J., 2013. Cryovolcanism on Titan: new results from Cassini RADAR and VIMS. *J. Geophys. Res.* 118 (3), 416–435. <https://doi.org/10.1002/jgre.20062>.
- McCord, T.B., Hayne, P., Combe, J.-P., Hansen, G.B., Barnes, J.W., Rodriguez, S., Le Mouélic, S., Baines, K.H., Buratti, B.J., Sotin, C., Nicholson, P., Jaumann, R., Nelson, R., 2008. The Cassini VIMS Team, Titan's surface: search for spectral diversity and composition using the Cassini VIMS investigation. *Icarus* 194, 212–242. <https://doi.org/10.1016/j.icarus.2007.08.039>.
- MacKenzie, S.M., Barnes, J.W., Sotin, C., Soderblom, J.M., Le Mouélic, S., Rodriguez, S., Baines, K.H., Buratti, B.J., Clark, R.N., Nicholson, P.D., McCord, T.B., 2014. Evidence of Titan's climate history from evaporte distribution, Shannon MacKenzie. et al., *Icarus* 243, 191–207. <https://doi.org/10.1016/j.icarus.2014.08.022>.
- Neish, C.D., Molaro, J.L., Lora, J.M., Howard, A.D., Kirk, R.L., Schenk, P., Bray, V.J., Lorenz, R.D., 2016. Fluvial erosion as a mechanism for crater modification on Titan. *Icarus* 270, 114–129. <https://doi.org/10.101/j.icarus.2015.07.022>.
- Pelkey, S.M., Mustard, J.F., Murchie, S., Clancy, R.T., Wolff, M., Smith, M., Milliken, R., Bilbring, J.-P., Gendrin, A., Poulet, F., Langevin, Y., Gondet, B., 2007. CRISM multi-spectral summary products: parameterizing mineral diversity on Mars from reflectance. *J. Geophys. Res.* 112, E08S14. <https://doi.org/10.1029/2006JE002831>.
- Porco, C.C., et al., 2005. Imaging of Titan with the Cassini spacecraft. *Nature* 434, 159–168.
- Radebaugh, J., Lorenz, R.D., Kirk, R.L., Lunine, J.I., Stofan, E.R., Lopes, R.M.C., Wall, S.D., The Cassini Radar Team, 2007. Mountains on Titan observed by Cassini Radar. *Icarus* 192 (1), 77–91. <https://doi.org/10.1016/j.icarus.2007.06.020>.
- Radebaugh, J., Lorenz, R.D., Lunine, J.I., Wall, S.D., Boubin, G., Reffet, E., Kirk, R.L., Lopes, R.M., Stofan, E.R., Soderblom, L., Allison, M., Janssen, M., Paillou, P., Callahan, P., Spencer, C., The Cassini RADAR Team, 2008. Dunes on Titan observed by Cassini RADAR. *Icarus* 194 (2), 690–703. <https://doi.org/10.1016/j.icarus.2007.10.015>.
- Rodriguez, S., Le Mouélic, S., Sotin, C., Clément, H., Clark, R.N., Buratti, B., Brown, R.H., McCord, T.B., Nicholson, P.D., Baines, K.H., The VIMS science team, 2006. Cassini/VIMS hyperspectral observations of the Huygens landing site on Titan. *Planet. Space Sci.* 54, 1510–1523.
- Rodriguez, S., Le Mouélic, S., Rannou, P., Sotin, C., Brown, R.H., Barnes, J.W., Griffith, C.A., Burgalat, J., Baines, K.H., Buratti, B.J., Clark, R.N., Nicholson, P.D., 2011. Titan's cloud seasonal activity from winter to spring with Cassini/VIMS. *Icarus* 216, 89–110. <https://doi.org/10.1016/j.icarus.2011.07.031>.
- Rodriguez, S., Le Mouélic, S., Rannou, S., Tobie, P., Baines, G., Barnes, K.H., Griffith, J.W., Hirtzig, C.A., Pitman, M., Sotin, C.K., Brown, C., Buratti, B.H., Clark, B.J., Nicholson, R.N., Global, P.D., 2009. Circulation as the main source of cloud activity on Titan. *Nature* 459, 678–682. <https://doi.org/10.1038/nature08014>.
- Rodriguez, S., Garcia, A., Lucas, A., Appérè, T., Le Gall, A., Reffet, E., Le Corre, L., Le Mouélic, S., Cornet, T., Courrech du Pont, S., Narvaez, C., Bourgeois, O., Radebaugh, J., Arnold, K., Barnes, J.W., Stephan, K., Jaumann, R., Sotin, C., Brown, R.H., Lorenz, R.D., Turtle, E.P., 2014. Global mapping and characterization of Titan's dune field with Cassini: Correlation between RADAR and VIMS observations. *Icarus* 230, 168–179. <https://doi.org/10.1016/j.icarus.2013.11.017>.
- Seignovert, B., 2015. Cassini Titan flyby [Data set]. Zenodo. <http://doi.org/10.5281/zenodo.155767>.
- Soderblom, L.A., Brown, R.H., Soderblom, J.M., Barnes, J.W., Kirk, R.L., Sotin, C., Jaumann, R., Mackinnon, D.J., Mackowski, D.W., Baines, K.H., Buratti, B.J., Clark, R.N., Nicholson, P.D., 2009a. The geology of Hotei Regio, Titan: correlation of Cassini VIMS and RADAR. *Icarus* 204 (2), 610–618. <https://doi.org/10.1016/j.icarus.2009.07.033>.
- Soderblom, L.A., Barnes, J.W., Brown, R.H., Clark, R.N., Janssen, M.A., McCord, T.B., Niemann, H.B., Tomasko, M.G., 2009b. Composition of Titan's Surface, book chapter in Titan: Cassini/Huygens, pp. 141–175.
- Soderblom, L.A., J.W. Barnes, L.A. Soderblom, R.H. Brown, C.A. Griffith, P.D. Nicholson, K. Stephan, R. Jaumann, C. Sotin, K.H. Baines, B.J. Buratti, R.N. Clark, Modeling specular reflections from hydrocarbon lakes on Titan, doi:[10.1016/j.icarus.2012.05.030](https://doi.org/10.1016/j.icarus.2012.05.030), 2012.
- Solomonidou, A., Coustenis, A., Hirtzig, M., Rodriguez, S., Stephan, K., Lopes, R.M.C.,

- Drossart, P., Sotin, C., Le Mouélic, S., Lawrence, K., Bratsolis, E., Jaumann, R., Brown, R.H., 2016. Temporal variations of Titan's surface with Cassini/VIMS. *Icarus* 270, 85–99. <https://doi.org/10.1016/j.icarus.2015.05.003>.
- Solomonidou, A., Coustenis, A., Lopes, R., Malaska, M., Rodriguez, S., Drossart, P., Elachi, C., Schmitt, B., Janssen, M., Hirtzig, M., Wall, S., Sotin, C., Lawrence, K., Altobelli, N., Bratsolis, N., Radabaugh, J., Stephan, K., Brown, R., Le Mouélic, S., Le Gall, A., Villanueva, E.V., Brossier, J.F., Bloom, A.A., Witasse, O., Matsoukas, C., Schoenfeld, A., 2018. The spectral nature of Titan's major geomorphological units: constraints on surface composition. *J. Geophys. Res.* 123 (2), 489–507. <https://doi.org/10.1002/2017JE005477>.
- Sotin, C., Jaumann, R., Buratti, B.J., Brown, R.H., Clark, R.N., Soderblom, L.A., Baines, K.H., Bellucci, G., Bibring, J.-P., Capaccioni, F., Cerroni, P., Combes, M., Coradini, A., Cruikshank, D.P., Drossart, P., Formisano, V., Langevin, Y., Matson, D.L., McCord, T.B., Nelson, R.M., Nicholson, P.D., Sicardy, B., Le Mouélic, S., Rodriguez, S., Stephan, K., Scholz, C.K., 2005. Release of volatiles from a possible cryovolcano from near-infrared imaging of Titan. *Nature* 786–789. <https://doi.org/10.1038/nature03596>.
- Sotin, C., Lawrence, K.J., Reinhardt, B., Barnes, J.W., Brown, R.H., Hayes, A.G., Le Mouélic, S., Rodriguez, S., Soderblom, J.M., Soderblom, L.A., Baines, K.H., Buratti, B.J., Clark, R.N., Jaumann, R., Nicholson, P.D., Stephan, K., 2012. Observations of Titan's northern lakes at 5 microns: Implications for the organic cycle and geology. *Icarus* 221 (2012), 768–786. <https://doi.org/10.1016/j.icarus.2012.08.017>.
- Stofan, E.R., et al., 2007. The lakes of Titan. *Nature* 445 (2007), 61–64. [https://doi.org/10.1016/S0019-1035\(03\)00125-8](https://doi.org/10.1016/S0019-1035(03)00125-8).
- Turtle, E.P., Perry, J.E., Barbara, J.M., Del Genio, A.D., Rodriguez, S., Le Mouélic, S., Sotin, C., Lora, J.M., Faulk, S., Corlies, P., Kelland, J., MacKenzie, S.M., West, R.A., McEwen, A.S., Lunine, J.I., Pitesky, J., Ray, T.L., Roy, M., 2018. Turtle et al. Titan's meteorology: Evidence for extensive subsurface methane reservoirs. *Geophys. Res. Lett.* 45 (11). <https://doi.org/10.1029/2018GL078170>, in review.
- Tomasko, M.G., et al., 2005. Rain, winds and haze during the Huygens probe's descent to Titan's surface. *Nature* 438, 765–778. <https://doi.org/10.1038/nature04126>.
- Vixie, G., Barnes, J.W., Bow, J., Le Mouélic, S., Rodriguez, S., Brown, R.H., Cerroni, P., Tosi, F., Buratti, B., Sotin, C., Filacchione, G., Capaccioni, F., Coradini, A., 2012. Mapping Titan's surface features within the visible spectrum via Cassini VIMS. *Planet. Space Sci.* 60, 52–61.
- Wood, C.A., Lorenz, R., Kirk, R., Lopes, R., Mitchell, K., Stofan, E., The Cassini RADAR Team, 2010. Impact craters on Titan. *Icarus* 206, 334–344.